Glass capillary microfluidics for production of monodispersed poly (dl-lactic acid) and polycaprolactone microparticles: experiments and numerical simulations

Journal of Colloid and Interface Science 418 (2014) 163–170

Contents lists available at ScienceDirect

Journal of Colloid and Interface Science

www.elsevier.com/locate/jcis

Glass capillary microfluidics for production of monodispersed poly (DL-lactic acid) and polycaprolactone microparticles: Experiments and numerical simulations

Goran T. Vladisavljević [a,*], Hamed Shahmohamadi [b], Diganta B. Das [a], Ekanem E. Ekanem [a], Zhandos Tauanov [a], Lav Sharma [a]

[a] Department of Chemical Engineering, Loughborough University, Loughborough LE11 3TU, United Kingdom
[b] Wolfson School of Mechanical and Manufacturing Engineering, Loughborough University, Loughborough LE11 3TU, United Kingdom

ARTICLE INFO

Article history:
Received 6 October 2013
Accepted 1 December 2013
Available online 6 December 2013

Keywords:
Drop microfluidics
Flow focusing
Poly(lactic acid)
Polycaprolactone
Monodispersed microparticle
Ultrasound contrast agent
Computational fluid dynamics
Porous particle
Lidocaine hydrochloride
Controlled drug release

ABSTRACT

Hypothesis: Droplet size in microfluidic devices is affected by wettability of the microfluidic channels. Three-dimensional countercurrent flow focusing using assemblies of chemically inert glass capillaries is expected to minimize wetting of the channel walls by the organic solvent.
Experiments: Monodispersed polycaprolactone and poly(lactic acid) particles with a diameter of 18–150 μm were produced by evaporation of solvent (dichloromethane or 1:2 mixture of chloroform and toluene) from oil-in-water or water-in-oil-in-water emulsions produced in three-dimensional flow focusing glass capillary devices. The drop generation behaviour was simulated numerically using the volume of fluid method.
Findings: The numerical results showed good agreement with high-speed video recordings. Monodispersed droplets were produced in the dripping regime when the ratio of the continuous phase flow rate to dispersed phase flow rate was 5–20 and the Weber number of the dispersed phase was less than 0.01. The porosity of polycaprolactone particles increased from 8 to 62% when 30 wt% of the water phase was incorporated in the organic phase prior to emulsification. The inner water phase was loaded with 0.156 wt% lidocaine hydrochloride to achieve a sustained drug release. 26% of lidocaine was released after 1 h and more than 93% of the drug was released after 130 h.

1. Introduction

Porous microparticles made from synthetic biodegradable polymers are increasingly being investigated for use in medical, biotechnological, and pharmaceutical applications in areas such as contrast-enhanced ultrasound imaging [1], controlled drug delivery [2] and cell growth in tissue engineering scaffolds [3]. Ultrasound is among the most popular medical imaging techniques used for visualizing subcutaneous body structures and blood flow [4]. However, with current technology, 20% of echocardiograms are unusable due to low contrast of the images. To address this issue, ultrasound contrast agents (UCA's) are increasingly being used with ultrasound to improve the quality of the images.

UCAs are intravenously administered gas-filled core–shell or matrix type microspheres with a lipid, protein or synthetic biodegradable polymer shell or matrix, which increases the backscattered signal from blood when insonified by low frequency ultrasound waves [1,5]. Targeted UCA's (TUCAs) may also be used for more specific molecular imaging [6], where particles are retained on the endothelium at the site of pathology via adhesion ligands incorporated into their surface [7]. TUCAs can be loaded with drugs to provide targeted non-invasive drug release on application of high frequency ultrasound [5,8].

Commercial UCAs have a relatively broad size distribution. For example, Optison® (GE Healthcare) has a mean particle diameter of 2.0–4.5 μm and a maximum diameter of 32 μm [9] while Definity® (Bristol-Myers Squibb Medical Imaging) has a mean particle diameter of 1.1–3.3 μm and a maximum diameter of 20 μm [9]. The resonant frequency of a capsule is directly related to its diameter. A capsule that is vibrated (using ultrasound) at its resonant frequency responds to ultrasonic excitation much more efficiently than one that is vibrated but not at its resonant frequency. Given that available ultrasound systems have limited frequency bandwidth, it is highly important that capsules have a narrow size distribution. In addition, monodispersed particles distribute more homogeneously in a patient's body, degrade in a more predictable way, and ensure a predictable therapeutic effect. Furthermore, capsules of the same size can supress the Ostwald ripening effect by reducing the Laplace pressure difference [10]. Therefore, there is

* Corresponding author. Fax: +44 1509223923.
E-mail address: g.vladisavljevic@lboro.ac.uk (G.T. Vladisavljević).

0021-9797/$ - see front matter © 2013 Elsevier Inc. All rights reserved.
http://dx.doi.org/10.1016/j.jcis.2013.12.002

a strong demand for UCAs and drug microcarriers with controllable size and a narrow particle size distribution.

Conventional methods for manufacturing UCAs such as spray drying [11], sonication or mechanical agitation [12] lead to polydisperse particles, due to the random nature of drop generation and breakup in atomization, mixing and cavitation processes. Monodispersed UCAs can be obtained by differential centrifugation of polydispersed particle population [13], ink-jet printing [14], microchannel emulsification [10–15], and co-axial electrohydrodynamic atomization [16], but these processes are either time-consuming and require multi-step processing or complex and relatively expensive. Monodispersed polymer particles can also be prepared using planar flow focusing microfluidic devices fabricated in polydimethylsiloxane (PDMS) by soft lithography [17,18]. In a planar (2D) flow focusing microfluidic device, the dispersed phase jet is forced through a rectangular orifice, where it is broken up into droplets due to high shear and pressure forces from the surrounding continuous phase. In this planar geometry, the dispersed phase contacts the orifice walls at low continuous phase flow rates (Fig. 1). However, surface wettability of PDMS can change after exposure to organic solvents. For example, extensive hydrophobic wetting of PDMS channels was noticed after exposure to dichloromethane [17]. In addition, due to its softness, PDMS channels are highly deformable.

In this work, monodisperse poly(lactic acid) (PLA) and polycaprolactone (PCL) microparticles with water droplets embedded within the polymer matrix were produced using a novel approach based on emulsification in a 3D (axisymmetric) flow focusing glass capillary device [19,20]. These particles can be used as intermediate products in the production of UCAs. The main objective was to investigate the effects of phase flow rates and geometry of the device on the droplet and particle size and droplet formation behaviour. In a 3D flow focusing device, the dispersed phase jet is completely surrounded by the continuous phase flow irrespective of the hydrodynamic conditions, due to circular orifice geometry (Fig. 1). Therefore, the organic phase does not make contact with the orifice and hydrophilic nature of the wall can be preserved [21]. Although glass capillary devices cannot be replicated as those made from mouldable polymers, they are more rigid and chemically stable than PDMS devices, have superior optical properties, low surface roughness and can be fabricated with a wide range of orifice sizes. In combination with the above experiments, we also developed a numerical model so that the drop size can be predicted for the given combination of system geometry, fluid flow rates and physical properties of fluids. The modelling results were used to better understand the mechanisms of drop generation.

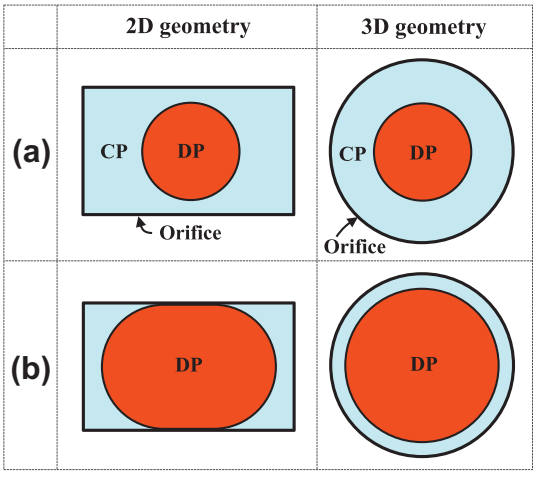

Fig. 1. Cross sectional view of a flow-focusing orifice showing the position of the dispersed phase (DP) in 2D and 3D microfluidic devices at: (a) high flow rate of the continuous phase (CP) and (b) low flow rate of the continuous phase. In the 2D device, the dispersed phase contacts the orifice wall at low continuous phase flow rates and the wall rapidly becomes hydrophobic. In the 3D device, the dispersed phase does not make contact with the orifice at any flow rate conditions and the orifice wall retains its hydrophilic properties.

2. Materials and methods

2.1. Materials for emulsion preparation

The oil phase in oil-in-water (O/W) emulsions was 1 wt% polycaprolactone (PCL, M_w = 14,000 g mol^{-1}, Sigma–Aldrich, UK) dissolved in dichloromethane (DCM, HPLC grade, Fisher Scientific, UK). The oil phase in water-in-oil-in-water (W/O/W) emulsions was a mixture of 1–3 wt% poly(DL-lactic acid) (PLA, M_w = 15,000 - g mol^{-1}, Polysciences, Inc., US) or polycaprolactone (PCL, M_w = 14,000 g mol^{-1}, Sigma–Aldrich, UK) dissolved in dichloromethane (DCM, HPLC grade, Fisher Scientific, UK) or 1:2 mixture of chloroform and toluene. 5–10 wt% polyglycerol polyricinoleate (PGPR, E476, Abitec Ltd., New Milton, UK) was added in the oil phase to prevent coalescence of inner water droplets, and 0.1–2 mM Nile red to help in visual identification of the particles. The inner water phase was Milli-Q water or 0.156 wt% lidocaine hydrochloride monohydrate (Sigma–Aldrich, UK). The continuous phase was 5 wt% aqueous solution of polyvinyl alcohol (PVA, M_w = 13,000–23,000 g mol^{-1}, 87–89% hydrolysed, Sigma–Aldrich, UK), pre-filtered by Whatman® Puradisc 30 syringe filters with 5 μm cellulose nitrate membrane. All chemicals were used as supplied. The physical properties of some of the fluids used in this work are listed in Table 1. The interfacial tension was measured using a Krüss DSA-100 pendant drop tensiometer.

2.2. Fabrication of microfluidic device

Microfluidic device was made up of two borosilicate glass capillary tubes where an inner capillary with a circular cross section (Intracel, Royston, UK, inner diameter 1 mm, outer diameter 580 μm) was inserted in an outer capillary with a square cross section (AIT Glass, Rockaway, US, inner dimension 1.05 mm) (Fig. 2a). One end of the the inner capillary was shaped into a tapering orifice with an inner diameter of 60–300 μm. First, a Flaming/Brown micropipette puller (P-97, Sutter Instrument Co., Linton Instrumentation, Norfolk, UK) was used to produce a sharp tip. The orifice diameter was then increased by sanding the tip against abrasive paper until the orifice with a required size and smooth rim was obtained. A microforge (MF-830, Intracel Ltd., Linton Instrumentation, Norfolk, UK) microscope was used to control the orifice size via a built-in scale (Fig. 2c). The capillary was flushed with water to remove any glass debris and treated with 2-[methoxy(polyethylenoxy)propyl]-trimethoxysilane (MPEOPS) (FluoroChem, Hadfield, UK) to enhance hydrophilicity of the glass surface. Subsequently, the treated round capillary was partly inserted into the square capillary and fixed in position onto a microscopic slide using epoxy resin adhesive (5-Minute Epoxy®, Devcon). Hypodermic needles with polypropylene hub (BD Precisionglide®, Sigma–Aldrich, UK) were glued over both ends of the square capillary to act as tube connectors for the continuous and dispersed phase, while the exposed end of the inner capillary was connected to a sampling vial.

2.3. Microfluidic experiments

Glass capillary device, placed on the stage of an inverted microscope (XDS-3, GX Microscopes, UK) was connected to gas tight SGE syringes via medical tubing (Fig. 2b). The continuous phase was pumped through polyethylene tubing, while the dispersed phase was supplied using polytetrafluoroethylene tubing to prevent

Table 1
Physical properties of dispersed phase and continuous phase used in this work. The interfacial tension of W/O droplets was measured against aqueous 5 wt% PVA solution.

Droplet composition	Density at 298 K (kg dm^{-3})	Viscosity at 298 K (mPa s)	Interfacial tension (mN m^{-1})
Pure DCM	1.32	0.416	2.4
1% PLA in DCM	1.34	0.480	2.4
W/O emulsion with 10 wt% water phase. The oil phase: 1% PLA + 10% PGPR in 1:2 chloroform/toluene	1.05	1.60	0.88
W/O emulsion with 20 wt% water phase. The oil phase: 1% PLA + 10% PGPR in DCM	1.24	1.29	1.6
5% PVA in water	1.02	4.04	–

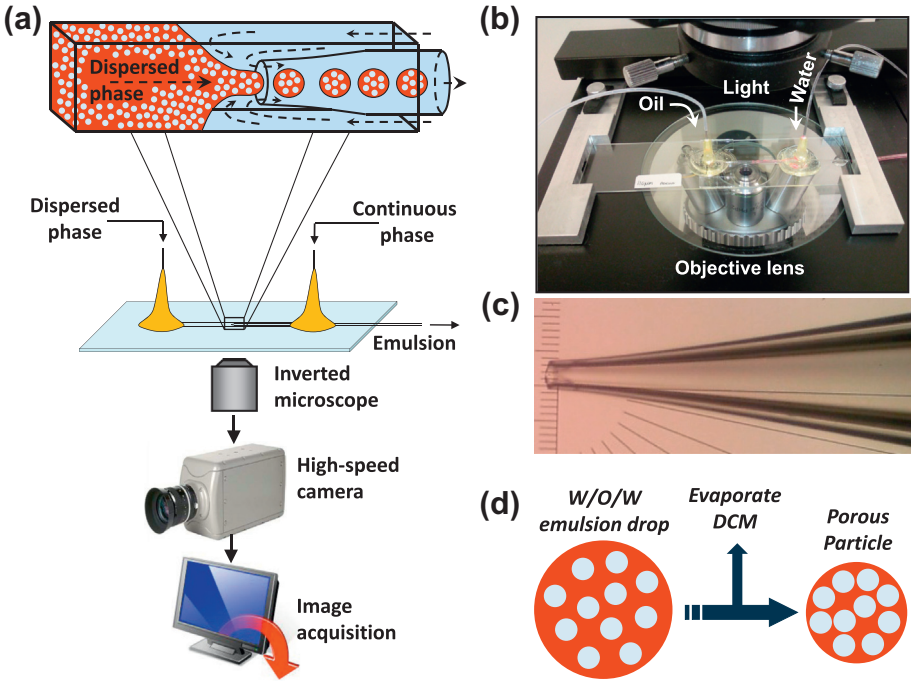

Fig. 2. (a) Schematic diagram of the experimental setup with a magnified view of W/O/W emulsion formation in the collection capillary of the microfluidic device; (b) microfluidic device placed on the microscope stage; (c) collection capillary with an orifice diameter of 60 μm. (d) formation of PLA particle with embedded inner water droplets from W/O/W emulsion droplet by solvent evaporation.

attack from DCM. Each phase was supplied into the device by a separate Harvard Apparatus 11 Elite syringe pump. The droplet formation was recorded using a Phantom V9.0 high-speed camera interfaced to a PC computer (Fig. 2a). High-speed images were analysed using ImageJ v.1.44 software (Wayne Rasband, National Institute of Health) to estimate droplet diameter, D_d and the frequency of droplet formation. Porous particles with water droplets embedded within a polymer matrix were formed by evaporating organic solvent from multiple emulsion droplets at room temperature in a vacuum oven for 30 min (Townson & Mercer, UK) (Fig. 2d). The particles were washed with deionized water to remove residual PVA. A primary water-in-oil (W/O) emulsion containing 10–30 wt% water phase was prepared by sonicating a W/O pre-mix using a Branson model 450 digital sonifier at an amplitude of 50% and a duty cycle of 0.2 s for 20 min in a closed vial submerged into the ice bath. High performance liquid chromatography (HPLC) (Agilent Technologies, 1100 series, Hewlett Packard) was used to analyse the amount of lidocaine hydrochloride in the continuous phase in drug release experiments.

2.4. Numerical modelling of droplet generation

2.4.1. Governing model equations

A computational fluid dynamics (CFD) based numerical simulation of the two-phase flow near the orifice was carried out. The equations of mass and momentum conservation for each liquid phase in the microfluidic device are as follows:

$$\frac{\partial \rho_{w,o}}{\partial t} + \nabla.\left(\rho_{w,o}\vec{v}_{w,o}\right) = 0 \quad (1)$$

$$\frac{\partial \rho_{w,o}\vec{v}_{w,o}}{\partial t} + \nabla.(\rho\vec{v}_{w,o}\vec{v}_{w,o}) = -\nabla p_{w,o} + \nabla.\left[\mu_{w,o}\left(\nabla\vec{v}_{w,o} + \nabla\vec{v}_{w,o}^{T}\right)\right] + \vec{F} \quad (2)$$

in which indices w and o denote water and oil phases, $\vec{v}$ and p are the fluid velocity vector and the pressure, respectively, ρ and μ are fluid density and viscosity, and $\vec{F}$ is the interfacial force.

The interface between water and oil phase was tracked using the volume of fluid (VOF) method [22] in which the following convection equation should be solved:

$$\frac{\partial \Omega}{\partial t} + \vec{v}.\nabla\Omega = 0 \quad (3)$$

where Ω is the function of the volume fraction. The implemented surface tension model was the continuum surface force (CSF) postulated by Brackbill et al. [23]. By means of this model, the interfacial tension was calculated and subsequently added to the momentum equation (Eq. (2)) as a source term. The interface unit normal ($\hat{n}$) and the curvature (κ) are defined as follows:

$$\hat{n} = \frac{\nabla\Omega}{|\nabla\Omega|} \text{ and } \kappa = -\left(\nabla . \hat{n}\right) \quad (4)$$

Therefore, the interfacial tension force in Eq. (2) can be expressed as:

$$\vec{F} = \sigma\kappa\frac{\nabla\Omega}{|\nabla\Omega|} \quad (5)$$

where σ is the interfacial tension between the dispersed and continuous phase.

2.4.2. Solution of governing model equations

For solving the system of equations, the commercial CFD package, namely, Fluent 14.0 (ANSYS Inc.) which is based on the finite volume method [24] was utilised. For this purpose, a model geometry as shown in Fig. 3(a) was constructed using ANSYS design modeler which was subsequently spatially discretised (meshed) by taking advantage of ANSYS meshing application. Hexahedral elements were used with the hexa-dominant meshing scheme. The entire flow domain was then meshed using approximately one million hexahedral cells (Fig. 3b). Preliminary runs were performed to ensure the independence of flow solution variables from mesh resolution. The lengths of the inlet channels were sufficiently long to assume fully developed laminar flow region for both phases prior to the inception of droplet generation. The outlet channel was constructed sufficiently long allowing the formation of more than one droplet in the region of interest in each run.

A segregated axisymmetric time-dependent solver was used along with the implicit body force formulation. The pressure interpolation scheme was chosen as PRESTO! (pressure staggering options), PISO (pressure-implicit with splitting of operators) scheme was used for pressure–velocity coupling, and the momentum equation is solved using a second order accurate scheme. Wall adhesion of the fluid particles was neglected and, hence, a zero contact angle ($\theta = 0$) was used in the simulations. As for the inlet boundary conditions, constant flow rates were applied for oil and water inlets. A pressure outlet boundary condition was implemented at the downstream where the gradients of all variables were set to zero in the normal direction. Non-slip boundary conditions are applied on all of the channel walls. Transient simulation with the method of VOF was conducted to track the pattern and behaviour of water–oil interface and to capture droplets formation. The physical properties of the fluids in Table 1 were used in the simulations.

3. Results and discussions

3.1. Numerical simulation of droplet formation and experimental verification

Fig. 4 illustrates simulated and experimental images of jet breakup in the dripping regime for two different orifice diameters, D_o (154 and 250 μm). Monodisperse droplets were formed in both cases and very good agreements between the simulated and high-speed video sequences were obtained at all time levels. For $D_o = 250$ μm, $Q_d = 1.2$ ml h^{-1} and $Q_c = 10$ ml h^{-1}, visible satellite droplets were formed between the two mother drops, as shown in Fig. 4(a–c). The size of the mother drops on the video recordings and simulations was very similar ($D_d \approx 240$ μm), although the shape of the interface was slightly different. The following mass balance equation can be used for the dispersed phase: $t_{drop} = 1/f = (D_d^3\pi/6)/Q_d$, where f is the frequency of drop generation and t_{drop} is the total drop formation time. Putting $d = 240 \times 10^{-6}$ m and $Q_d = 3.333 \times 10^{-10}$ m^3 s^{-1} into the above equation, one obtains $t_{drop} = 0.022$ s and $f = 46$ Hz which is in good match with experimental and simulation results in Fig. 4(a–c). Similarly, a good agreement between the experimental and simulation results was achieved for the smaller orifice size, as shown in Fig. 4(d–f). These results provide the confidence that the developed numerical method is able to accurately model the drop generation behaviour in the microfluidic system.

The drop detachment point on high-speed video frames shown in Fig. 4(a–c) is located $0.7D_o$ downstream of the orifice. At $t = 1$ ms, the tip of the dispersed phase retracted to $L \approx 0.3D_o$, causing a highly extended thread to collapse from the tip of the dispersed phase finger, leaving a satellite droplet (Fig. 4a). The tip of the dispersed phase is conical after collapse of the thread, but the interface quickly regains a hemispherical shape due to the action of interfacial tension minimizing the surface area. In the next 8 ms (from $t = 1$ to $t = 9$ ms), the tip of the dispersed phase grows until it reaches a maximum width at the entry section of the orifice of $W \approx 0.57D_o$ (Fig. 4b). In the time interval from 9 to 12 ms, the dispersed phase jet moves downstream, while keeping its width constant at the entry section. From $t = 12$ ms onward, the necking process occurs, characterised by thinning of the jet and formation of a neck. At $t = 21$ ms, the necking region is located $0.42D_o$ downstream of the orifice and the flow of the continuous phase stretches the emerging droplet into an elongated shape (Fig. 4c). The neck ruptures at $t = 22$ ms to complete the droplet formation process and the whole process starts again.

Fig. 5 is based entirely on numerical results which shows (a) the velocity contours (velocity magnitude) and vectors and (b) pressure distribution along the horizontal plane of symmetry at $Q_d = 1.2$ ml h^{-1}, $Q_c = 10$ ml h^{-1}, $D_o = 250$ μm, and $t = 21$ ms. The maximum velocity of the aqueous phase was observed at the four corners between the inner and outer capillary. The maximum velocity of the aqueous phase inside the orifice was at the entry section due to its minimum cross-sectional area (Fig. 5a). The average velocity of the aqueous phase at the entrance of the orifice was much higher than that of the dispersed phase causing a viscous drag force at the interface to pull the dispersed phase downstream. The velocity of the aqueous phase decreased at the neck region and then increased further downstream due to a reduced cross-sectional area for the flow caused by the presence of a droplet. A fully developed parabolic velocity profile was established at a sufficient distance downstream with a maximum velocity in the centre of the capillary and insignificant difference in velocity between the droplets and the surrounding continuous phase liquid.

The distribution of pressure in the device is shown in Fig. 5b. The pressure inside the droplets was greater than that in the surrounding aqueous phase, due to the interfacial tension. A pressure gradient across the orifice in the direction of flow forced both

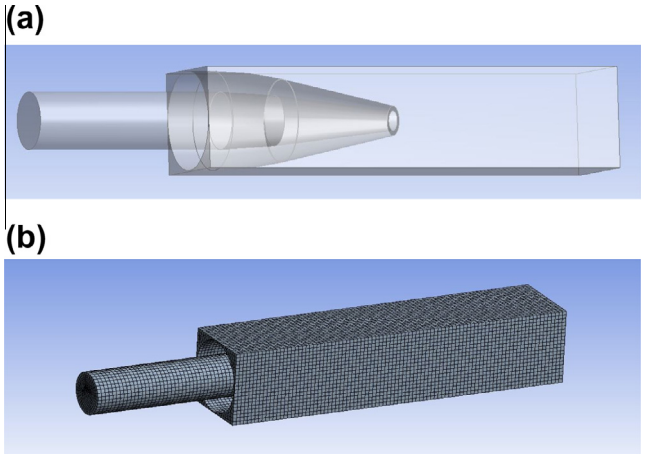

Fig. 3. (a) The model geometry of flow focusing microcapillary device constructed using ANSYS design modeler and (b) Hexahedral mesh used to discretise the computational domain.

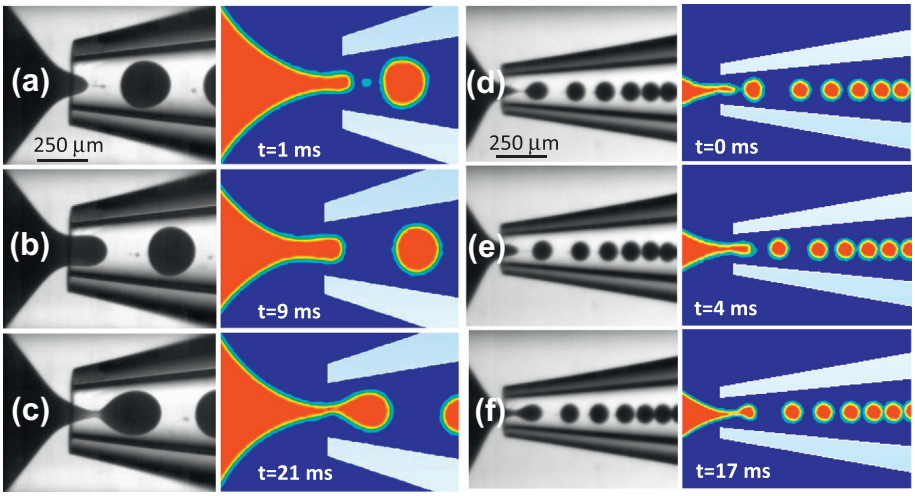

Fig. 4. High-speed video frames and CFD simulations of drop breakup sequence. The organic solvent was DCM and the polymer was PLA. (a–c): Q_d = 1.2 ml h^{-1}, Q_c = 10 ml h^{-1}, the D_o = 250 μm, D_d = 240 μm, and t_{drop} = 22 ms; (d–f): Q_d = 0.07 ml h^{-1}, Q_c = 0.42 ml h^{-1}, the D_o = 154 μm, D_d = 90 μm, and t_{drop} = 19 ms. The time t = 0 corresponds to the moment of pinch-off (D_o – orifice diameter, D_d – droplet diameter, t_{drop} – droplet formation time).

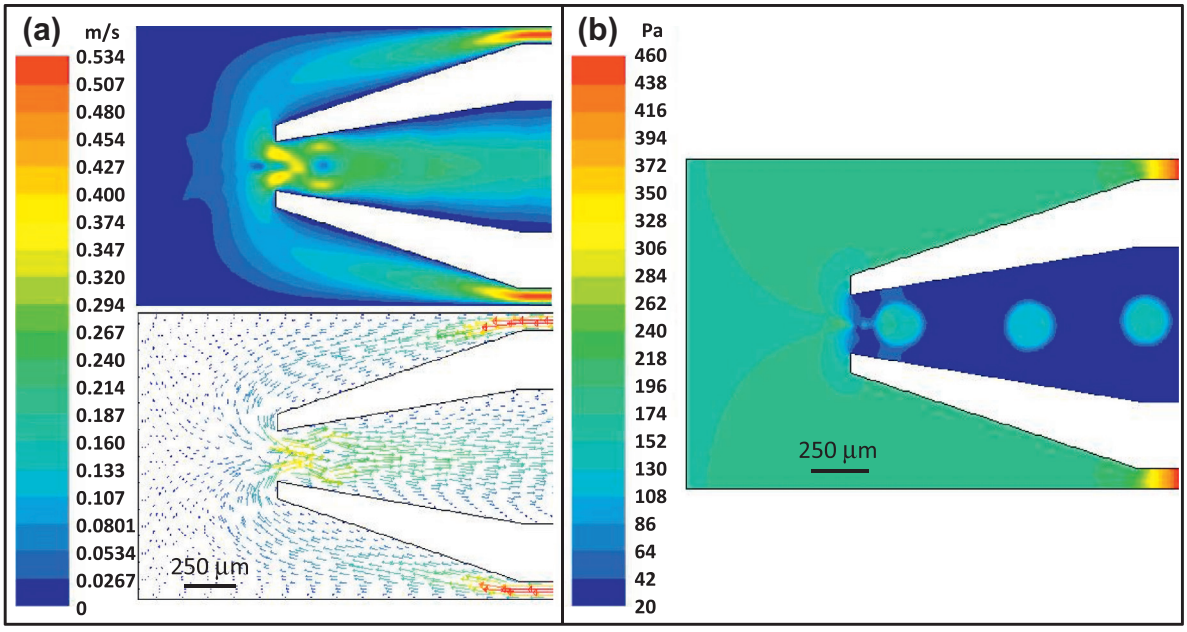

Fig. 5. (a) Velocity contours and vectors and (b) pressure distribution in the flow focusing capillary device along the horizontal plane of symmetry as predicted by the CFD simulation performed at D_o = 250 μm, Q_d = 1.2 ml/h, Q_c = 10 ml/h and t_{drop} = 21 ms.

liquid streams into the orifice. In addition, a build-up of pressure was noticeable in the aqueous phase between the emerging droplet and the wall resulting from the high resistance to flow of the continuous phase in the thin annular film that separate the droplet from the wall of the capillary. Similar phenomenon was also observed in planar T-junctions [25].

3.2. Experiments on droplet formation behaviour as a function of fluid flow rates and orifice size

The droplet size and generation rate were precisely controlled by the phase flow rates and the orifice size, as shown in Fig. 6. It can be noticed that the spacing between the droplets was progressively smaller as they moved through the collection tube, which was due to the decreasing velocity of the continuous phase as a result of tapered shape of the collection tube. In Figs. 6a-d, the orifice diameter D_o was constant at 175 μm, but the size of the droplets varied significantly as a result of variations in Q_c/Q_d and Q_d. In Figs. 6 a-b, the dripping regime occurred because Q_c/Q_d was in the optimum range for dripping regime of 5–20 and Q_d was low. As a result, the drag force was insufficient to stretch the dispersed phase into a long jet, but high enough to keep the droplet size considerably smaller than the orifice size. In addition, the inertial force of the dispersed phase was negligible due to low Q_d. In the dripping regime, the resultant droplet size is a result of competition between the drag force pulling the dispersed phase downstream and the interfacial tension force acting in the opposite direction. This force balance is given by [26]: $\mu_c u_c D_d \approx D_{neck}\sigma$, where u_c is the mean velocity of the continuous phase past the droplet and D_{neck} is the neck diameter. The drop size in the dripping regime decreased as Q_c/Q_d increased, which can be explained by the higher drag force, a behaviour found previously in the formation of O/W emulsions [27,28]. In Fig. 6c, the droplets were formed in the so-called geometry-controlled [29] or squeezing [30] regime, because

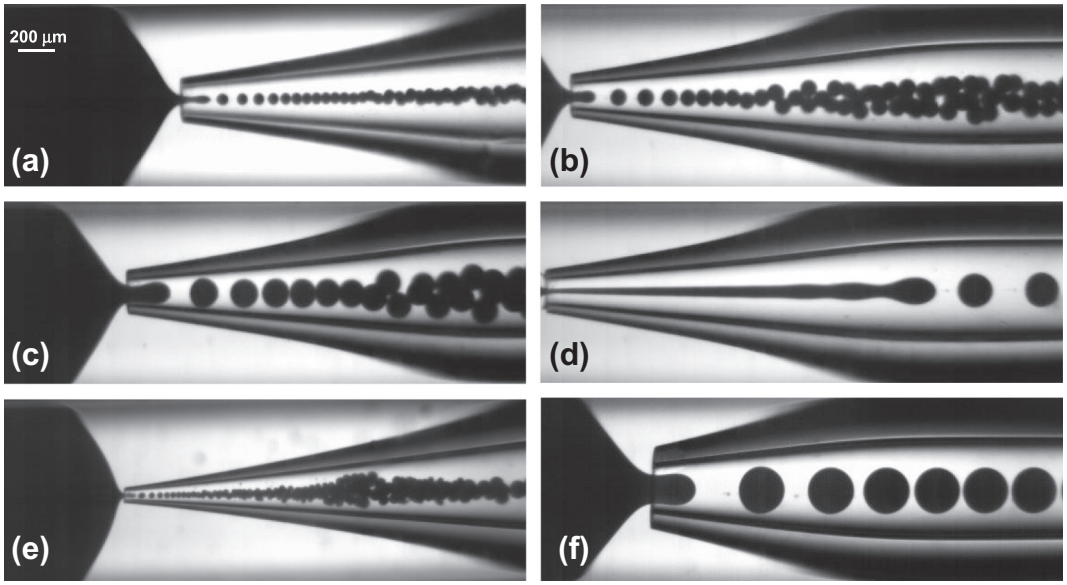

Fig. 6. Micrographs showing formation of PLA/organic solvent droplets: (a) Q_c = 0.36 ml h^1, Q_d = 0.023 ml h^{-1}, D_o = 175 μm, D_d = 66 μm, f = 43 Hz (see also Video V1 in the supplementary material section), 10% PGPR; (b) Q_c = 0.84 ml h^1, Q_d = 0.13 ml h^{-1}, D_o = 175 μm, D_d = 110 μm, f = 51 Hz, 5% PGPR; (c) Q_c = 0.44 ml h^1, Q_d = 0.14 ml h^{-1}, D_o = 175 μm, D_d = 175 μm, f = 18 Hz, 5% PGPR; (d) Q_c = 5 ml h^1, Q_d = 0.41 ml h^{-1}, D_o = 175 μm, D_d = 208 μm, f = 24 Hz, 5% PGPR; (e) Q_c = 0.035 ml h^1, Q_d = 0.004 ml h^{-1}, D_o = 60 μm, D_d = 34 μm, f = 55 Hz, 10% PGPR; (f) Q_c = 10 ml h^1, Q_d = 1.9 ml h^{-1}, D_o = 318 μm, D_d = 290 μm, f = 41 Hz, 10% PGPR. The same scale bar applies to all images. The organic solvent was 1:2 (v/v) mixture of chloroform and toluene in figures (a–e) and DCM in figure (f). The PLGA concentration in the organic phase was 5–10 wt%.

Q_c/Q_d was 3, which was below the lower critical value for the dripping regime and thus, the drag force exerted by the continuous phase was small compared to the interfacial tension force. Under this regime, the jet grows in the collection tube until it occupies almost the entire cross section. To drive the flow of the aqueous phase through a narrow space between the wall of the capillary and the emerging drop, a higher pressure was required in the continuous phase stream. The higher upstream pressure of the continuous phase squeezed the neck until a breakup occurred. The droplet detachment happens once the sum of the drag force and the squeezing pressure exceeds the capillary pressure. As shown in Fig. 6c, the size of the released drop was very similar to the orifice size, which was a feature found previously in planar flow focusing devices [31].

In Fig. 6d, the droplets were formed in the jetting regime, because Q_d was above the upper critical value for the dripping regime, although Q_c/Q_d was within the optimum range. In the dripping regime, the droplet detachment region was within 1.5 orifice diameters downstream of the orifice and was gradually moved downstream as Q_c/Q_d was increased. In the jetting regime, the detachment region was located at $L = 14D_o$ downstream. In this case, the mean velocity of the dispersed phase in the orifice was higher than that of the surrounding aqueous phase (u_d = 0.10 and u_c = 0.06 m s^{-1}). As a result, the drop size is determined by the balance between the inertial force of the dispersed phase and the interfacial tension force; a ratio of these two forces is given by the Weber number of the dispersed phase: $W_d = \rho_d D_j u_d^2/\sigma$, where ρ_d is the dispersed phase density, D_j is the jet diameter, and u_d is the mean velocity of the dispersed phase. At $W_d < 0.01$ ($W_d = 5 \times 10^{-4}$ and 4×10^{-3} in Fig. 6a and b, respectively), the inertial force is small compared to interfacial tension and the dripping regime prevails. At $W_d > 0.1$ (W_d = 0.45 in Fig. 6d), the inertial force dominates the interfacial tension, leading to jetting. In fact, the sum of all forces acting in the direction of flow must ultimately overcome interfacial tension force to cause the transition from dripping to jetting. Therefore, the dripping-jetting transition is governed by the sum $W_d + Ca_c$, where Ca_c is the capillary number of the continuous phase, given by $Ca_c = \mu_c u_c/\sigma$. In Fig. 6d, Ca_c = 0.28 and $W_d + Ca_c$ = 0.73. In co-flow glass capillary devices,

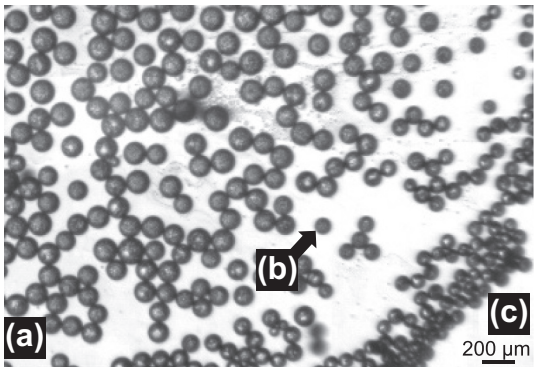

Fig. 7. Optical micrograph showing formation of PLA micro-particles, containing water droplets embedded within a polymer matrix, being formed from double emulsion droplets by DCM evaporation: (a) initial double emulsion droplets (D_d ≈134 μm); (b) partly-evaporated droplets; (c) completely evaporated particles (D_p ≈ 81 μm). The amount of inner water phase in the middle phase: 10 wt%, the middle phase: 1 wt% PLA + 10 wt% PGPR in DCM.

the transition from dripping to jetting at Ca_c = 0.28 was found to occur at W_d = 0.3–2, depending on the viscosity ratio μ_d/μ_c [26], which is within the range of critical Weber number in this work.

Fig. 6e–f demonstrate the capability of our device to generate very large or small droplets using relatively small or large orifice size. In both figures, the flow rate ratio was within the optimum range and the Weber number of the dispersed phase was sufficiently low, resulting in the dripping regime and monodispersed droplets generation.

3.3. Formation of biodegradable micro-particles by solvent evaporation

Assuming a complete DCM evaporation and 100% encapsulation yield of inner water droplets within the polymer matrix, the particle volume after DCM evaporation is given by:

$$V_p = \frac{x_p \rho_d}{\rho_p} V_d \tag{6}$$

where x_p is the mass ratio of non- or less volatile compounds in the droplet phase, ρ_p is the particle density after DCM evaporation, and ρ_d is the droplet density. Non- or less volatile compound means any compound except DCM. From Eq. (6):

$$D_p = \sqrt[3]{\frac{x_p \rho_d}{\rho_p}} D_d \tag{7}$$

where D_p is the particle diameter. For the conditions in Fig. 7: $x_p = 0.2$, $\rho_p = 985$ kg m^{-3}, and $\rho_d = 1240$ kg m^{-3}. Putting these values into Eq. (7) gives $D_p = 85$ μm. A small difference between the theoretical and experimental value of the particle diameter can be attributed to the release of inner water droplets into the outer aqueous phase during DCM evaporation. A complete release of the inner water droplets would lead to the particle diameter of 67 μm, which means that the encapsulation yield of inner droplets was almost 80%.

Fig. 8 shows a relationship between the droplet diameter and particle diameter for PCL particles formed by DCM evaporation from the droplets containing 1 wt% PCL and 5 wt% PGPR in the organic phase. The particle size was significantly smaller when the organic solvent evaporated from O/W than multiple (W/O/W) emulsion, which can be attributed to the presence of inner water droplets within the polymer matrix. The dash-dot lines in Fig. 8 represent the predicted droplet-particle relationship for zero particle porosity ($\varepsilon = 0$). The line of zero porosity for multiple emulsion has a higher slope, due to the presence of surfactant (PGPR) in the particle structure. When PCL particles were formed from single emulsion, the particle size was only slightly higher than that theoretically predicted for zero particle porosity, revealing that the particle porosity was rather low. The theoretical gradient of the D_p vs. D_d line for single emulsion is equal to: $(\partial D_p/\partial D_d)_{theor} = \sqrt[3]{x_{PCL}\rho_d/\rho_{PCL}}$, where $\rho_d = 1343$ kg m^{-3} is the density of the droplet phase, $\rho_{PCL} = 1145$ kg m^{-3} is the density of PCL, and $x_{PCL} = 0.01$ is the mass fraction of PCL in the organic phase. From the ratio of the theoretical gradient to the experimental gradient of the D_p vs. D_d line, the particle porosity of $\varepsilon = 8\%$ was deduced using the equation:

$$\varepsilon = 1 - \left[\frac{(\partial D_p/\partial D_d)_{theor}}{(\partial D_p/\partial D_d)_{exp}}\right]^3 \tag{8}$$

where $(\partial D_p/\partial D_d)_{theor} = 0.2272$ and $(\partial D_p/\partial D_d)_{exp} = 0.2340$, respectively. A discrepancy between the theoretical and experimental line

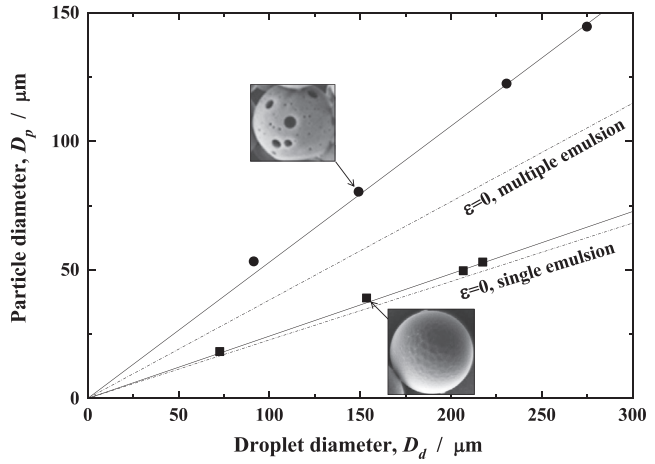

Fig. 8. A relationship between the particle diameter and droplet diameter for PCL particles prepared from droplets containing 1 wt% PCL in the organic phase: ● experimental data for multiple emulsion; ■: experimental data for single emulsion. Dashed lines are theoretical lines for zero particle porosity, constructed using mass balance equations. SEM images of particles obtained using single and multiple emulsions are also shown.

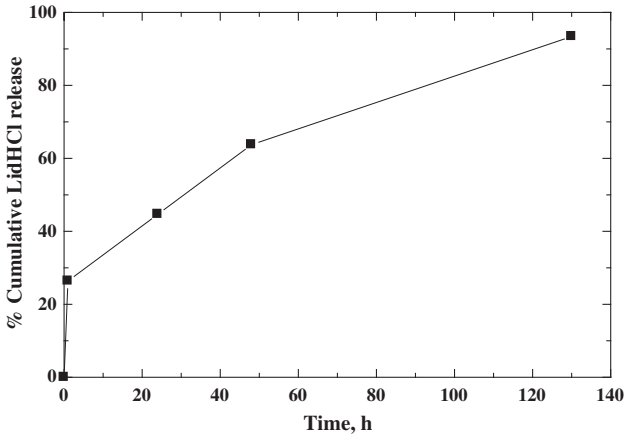

Fig. 9. The release profile of lidocaine hydrochloride (LidHCl) from inner water droplets embedded within PCL microparticles. The initial concentration of LidHCl in the inner water phase was 0.156 wt% and the amount of inner water phase in the organic phase was 30 wt%.

is significant for multiple emulsion, indicating that the particles formed from multiple emulsion were more porous ($\varepsilon = 62\%$). Ultrasound-responsive biodegradable particles can be fabricated by freeze-drying these porous PCL particles, followed by loading a gas (e.g. perfluorocarbons) within the pores formed by evaporated water phase. Particles produced in this work can be used for subcutaneous injection. For intravenous administration, the particle size should be 1–5 μm, which means that the maximum size of multiple emulsion droplets should be about 10 μm and the maximum size of the collection capillary should be about 20 μm.

3.4. Loading and release of drugs

The inner water phase can be loaded with a hydrophilic drug to achieve a sustained or even triggered drug release into the outer aqueous phase. Fig. 9 shows *in vitro* release profile of lidocaine hydrochloride (LidHCl) from PCL particles containing 0.156 wt% of LidHCl loaded in the inner water phase. Lidocaine is a hydrophobic local anesthetic but LidHCl is a weakly acidic, hydrophilic molecule which is readily soluble in water at ambient temperature. Lidocaine is widely used in the treatment of both acute and chronic pain, but its performance is limited by the short duration of action. On the other hand, if added in large quantities, lidocaine exhibits a number of harmful side effects, such as drowsiness, tinnitus, twitching, and even seizures. Therefore, there is a strong need for drug delivery vehicles that can release lidocaine over prolonged time, while keeping its plasma concentration at the optimum level [32]. The results show that 26.3% of lidocaine was released within the first 1 h following the particles production, probably due to initial burst as a result of partial release of inner water droplets during DCM evaporation. After the initial burst release, the remaining amount of LidHCl was slowly released over a long period of time, so that only 44.7% of LidHCl was released after 24 h. After 130 h, the drug was almost completely released to the outer aqueous phase with less than 7% of the drug remaining within the particles. These results indicate that controlled release of hydrophilic drugs can be achieved by their encapsulation within water droplets embedded within PCL particles.

4. Conclusions

We have developed a cheap and reliable microfluidic method for controllable production of biodegradable microparticles based on countercurrent flow focusing in a glass capillary device and

solvent evaporation. The process is suitable for production of monodisperse droplets and particles over a wide range of sizes and does not suffer from surface wetting problems found in planar flow focusing devices [17]. It was attributed to 3D design of the flow focusing orifice and hydrophilic pre-treatment of the glass surface with an organosilane (MPEOPS). Monodispersed droplets were formed in dripping regime which prevailed at Q_c/Q_d between 5 and 20 and the Weber numbers of the dispersed phase less than 10^{-2}. The droplet size was controlled by the fluid flow rates and the orifice size. The particle porosity was tuned by dispersing the water phase in the organic solution prior to emulsification in the microfluidic device. Biodegradable matrix-type polymeric particles with embedded water droplets developed in this work can be freeze-dried and loaded with an inert gas to produce ultrasound contrast agents for medical sonography or molecular imaging [6]. We have loaded inner water droplets with a hydrophilic drug (lidocaine hydrochloride) to achieve a sustained drug release over a period of 130 h. The fabrication process developed in this work can be used for the production of wide range of monodisperse matrix-type microcapsules by emulsification–solvent evaporation [33], such as solid lipid particles, 3D colloidal assemblies, Janus particles and silica particles.

In combination with the experimental work a numerical model of drop generation in 3D flow focusing devices was developed. The numerical results were compared with the experimental results and a good match was obtained. The numerical modelling was useful to reveal distribution of fluid pressure and velocity in the device and thus to better understand the mechanism of drop generation in the dripping regime. A build-up of pressure was noticeable between the emerging droplet and the wall resulting from the high resistance to flow of the continuous phase and similar phenomenon was observed in planar T-junction devices [25].

Acknowledgment

The work was supported by the Engineering and Physical Sciences Research Council (EPSRC) of the United Kingdom (grant reference number: EP/HO29923/1). The authors thank Dr John Henry for his assistance in the analysis of video footages.

Appendix A. Supplementary material

Supplementary data associated with this article can be found, in the online version, at http://dx.doi.org/10.1016/j.jcis.2013.12.002.

References

[1] D. Cosgrove, Eur. J. Radiol. 60 (2006) 324–330.
[2] F. Ito, H. Fujimori, H. Honnami, H. Kawakami, K. Kanamura, K. Makino, J. Mater Sci. 21 (2010) 1563–1571.
[3] S.K. Sahoo, A.K. Panda, V. Labhasetwar, Biomacromolecules 6 (2005) 1132–1139.
[4] J.J.P. Kastelein, E. de Groot, Eur. Heart J. 29 (2008) 849–858.
[5] M.R. Böhmer, A.L. Klibanov, K. Tiemann, C.S. Hall, H. Gruell, O.C. Steinbach, Eur. J. Radiol. 70 (2009) 242–253.
[6] A.L. Klibanov, J. Nucl. Cardiol. 14 (2007) 876–884.
[7] J.J. Rychak, B. Li, S.T. Acton, A. Leppänen, R.D. Cummings, K. Ley, A.L. Klibanov, Mol. Pharm. 3 (2006) 516–524.
[8] J.D. Lathia, L. Leodore, M.A. Wheatley, Ultrasonics 42 (2004) 763–768.
[9] N. McDannold, N. Vykhodtseva, K. Hynynen, Ultrasound Med. Biol. 33 (2006) 584–590.
[10] M. Yasuno, S. Sugiura, S. Iwamoto, M. Nakajima, A. Shono, K. Satoh, AIChE J. 50 (2004) 3227–3233.
[11] J.A. Straub, D.E. Chickering, C.C. Church, B. Shah, T. Hanlon, H. Bernstein, J. Controlled Release 108 (2005) 21–32.
[12] S.B. Feinstein, P.M. Shah, R.J. Bing, S. Meerbaum, E. Corday, B.L. Chang, G. Santillan, Y. Fujibayashi, J. Am. Coll. Cardiol. 4 (1984) 595–600.
[13] J.A. Feshitan, C.C. Chen, J.J. Kwan, M.A. Borden, J. Colloid Interface Sci. 329 (2009) 316–324.
[14] M.R. Böhmer, R. Schroeders, J.A.M. Steenbakkers, S.H.P.M. de Winter, P.A. Duineveld, J. Lub, W.P.M. Nijssen, J.A. Pikkemaat, H.R. Stapert, Colloids Surf., A 289 (2006) 96–104.
[15] G.T. Vladisavljević, I. Kobayashi, M. Nakajima, Microfluidic. Nanofluidic. 10 (2011) 1199–1209.
[16] U. Farook, H.B. Zhang, M.J. Edirisinghe, E. Stride, N. Saffari, Med. Eng. Phys. 29 (2007) 749–754.
[17] Q. Xu, M. Hashimoto, T.T. Dang, T. Hoare, D.S. Kohane, G.M. Whitesides, R. Langer, D.G. Anderson, Small 5 (2009) 1575–1581.
[18] G.T. Vladisavljević, N. Khalid, M.A. Neves, T. Kuroiwa, M. Nakajima, K. Uemura, S. Ichikawa, I. Kobayashi, Industrial lab on a chip: design, applications and scale up for drug discovery and delivery, Adv. Drug Deliv. Rev., (doi: 10.1016/j.addr.2013.07.017).
[19] R.K. Shah, H.C. Shum, A.C. Rowat, D. Lee, J.J. Agresti, A.S. Utada, L.Y. Chu, J.W. Kim, A. Fernandez-Nieves, C.J. Martinez, D.A. Weitz, Designer Emulsions Using Microfluidics 11 (2008) 18–27.
[20] W.J. Duncanson, T. Lin, A.R. Abate, S. Seiffert, R.K. Shah, D.A. Weitz, Lab Chip 12 (2012) 2135–2145.
[21] S. Takeuchi, P. Garstecki, D.B. Weibel, G.M. Whitesides, Adv. Mater. 17 (2005) 1067–1072.
[22] C.W. Hirt, B.D. Nichols, J. Comput. Phys. 39 (1981) 201–225.
[23] J.U. Brackbill, D.B. Kothe, C. Zemach, J. Comput. Phys. 100 (1992) 335–354.
[24] R. Eymard, T. Gallouët, R. Herbin, The finite volume method Handbook of Numerical Analysis VII (2000) 713–1020.
[25] P. Garstecki, M.J. Fuerstman, H.A. Stone, G.M. Whitesides, Lab Chip 6 (2006) 437–446.
[26] A.S. Utada, A. Fernandez-Nieves, H.A. Stone, D.A. Weitz, Phys. Rev. Lett. 99 (2007) 094502.
[27] G.T. Vladisavljević, W.J. Duncanson, H.C. Shum, D.A. Weitz, Langmuir 28 (2012) 12948–12954.
[28] G.T. Vladisavljević, J.V. Henry, W.J. Duncanson, H.C. Shum, D.A. Weitz, Progr. Colloid Polym. Sci. 139 (2012) 111–114.
[29] M. De Menech, P. Garstecki, F. Jousse, H.A. Stone, J. Fluid Mech. 595 (2008) 141–161.
[30] S.L. Anna, H.C. Mayer, Phys. Fluids 18 (2006) 121512.
[31] G.T. Vladisavljević, I. Kobayashi, M. Nakajima, Microfluid. Nanofluid. 13 (2012) 151–178.
[32] A. Nayak, D.B. Das, G.V. Vladisavljević, Microneedle assisted permeation of lidocaine carboxymethylcellulose with gelatine co-polymer hydrogel, Pharm. Res., doi: 10.1007/s11095-013-1240-z (in press).
[33] P.J. Watts, M.C. Davies, C.D. Melia, Crit. Rev. Ther. Drug Carrier Syst. 7 (1990) 235–259.